

# We are IntechOpen, the world's leading publisher of Open Access books Built by scientists, for scientists

6,900

Open access books available

186,000

International authors and editors

200M

Downloads

Our authors are among the

154

Countries delivered to

TOP 1%

most cited scientists

12.2%

Contributors from top 500 universities



WEB OF SCIENCE™

Selection of our books indexed in the Book Citation Index  
in Web of Science™ Core Collection (BKCI)

Interested in publishing with us?  
Contact [book.department@intechopen.com](mailto:book.department@intechopen.com)

Numbers displayed above are based on latest data collected.  
For more information visit [www.intechopen.com](http://www.intechopen.com)



---

# X-Ray Spectroscopy — The Driving Force to Understand and Develop Catalysis

---

Jakub Szlachetko and Jacinto Sá

Additional information is available at the end of the chapter

<http://dx.doi.org/10.5772/61940>

---

## Abstract

Catalysis is involved in about 90% of manmade chemicals. The development of novel or improved catalysts requires fundamental understanding of the commanding steps of a catalytic reaction. In simple terms, a catalytic transformation depends on the coupling between catalyst electronic structure and reagents' molecular orbitals. Herein, we report a spectroscopic technique capable of determining the electronic structure of metal containing catalysts under working conditions. The technique is called photon-in photon-out X-ray spectroscopy and can be employed to characterize materials, unveil substrate adsorption parameters, and follow changes in electronic structure during catalytic reactions.

**Keywords:** Photon-in photon-out X-ray spectroscopy, Electronic structure, Spectroscopy under working conditions

---

## 1. Introduction

Catalysis is a fascinating field located at the edge of a multitude of disciplines and fields. Spectroscopy dedicated to understanding catalytic phenomenon is among the most active research areas in field. The ability to visualize a catalytic transformation in real time has lured scientists due to the technical challenges and the potential for unprecedented understanding. The importance in accessing fundamental understanding of catalysis was masterfully highlighted in the 2007 report of the US Department of Energy, Basic Energy Sciences Workshop [1]: *To realize the full potential of catalysis for energy applications, scientists must develop a profound understanding of catalytic transformations so that they can design and build effective catalysts with atom-by-atom precision and convert reactants to products with molecular precision. Moreover, they must build tools to make real-time, spatially resolved measurements of operating catalysts. Ultimately,*

---

*scientists must use these tools to achieve a fundamental understanding of catalytic processes occurring in multiscale, multiphase environments.* However, this is applicable for any kind of catalytic system.

At its most fundamental level, catalysis is directly related to the electronic structure of the valence shells because they control chemical bond formation/rupture [2]. Several spectroscopies can provide information on valence shells but only X-rays do it directly. Hard X-rays are the epitome of spectroscopic probes because of their great penetration depth, and element specificity, which enables studies of catalytic states under working conditions [3]. X-ray photon-in photon-out core level spectroscopy is a powerful tool to understand catalytic reactions because it enables us to map the entire electronic structure of the catalyst under catalytic relevant conditions.

In this book chapter, we summarize our latest efforts in the use of synchrotron-based high-resolution X-ray spectroscopy to study a plethora of academic and industrial relevant catalytic systems. We will start by covering in a succinct manner the developments in the field that allow for the understanding of catalysis *in situ/operando* and time-resolved, keeping the high-energy resolution and element specificity. This section includes an overview on techniques, spectrometers, and experimental setups. After that we will describe the studies we carried out to understand catalysis and materials. Our work spans over three fundamental aspects of catalysis:

- a. Materials characterization
- b. Molecular adsorption
- c. Study of catalytic reactions under real working conditions (*in situ*).

Vast majority of the studies were carried out on a dispersive von Hamos-type spectrometer [4]; however, when a higher peak-to-background signal level was necessary the experiments were carried out with a Johann-type spectrometer [5]. The studies were carried out both in homogeneous and heterogeneous catalytic systems. The latest includes also studies on photocatalysis.

The future of this spectroscopy concerns its application at the X-ray free electron lasers (XFELs). The advent of XFELs enabled scientist to achieve the goal of producing a movie of a catalytic transformation. XFEL light sources are in its beginning but their effect on the field of time-resolved X-ray science will be deep and comprehensive because reactions can be followed not only *in situ* but also in real time, this of course if the current limitations in respect to selective triggering and sample stability are overcome. Quoting Sá & Szelachetko: *in a cinematographic analogy, we have the camera (von Hamos Spectrometer), the film (HEROS), the set (catalytic reactor), the script (catalytic reaction) and the actors (catalyst and reagent molecules); what is missing is the director to shout 'action' and direct the scenes (pulse shaping), and that the actors do not fall ill (sample refreshment)* [6]. The insights gathered from the high-resolution X-ray spectroscopy provide deeper understanding of the systems and reactions, which can be used to improve or develop novel catalysts with enhanced properties.

## 2. Photon-in photon-out X-ray spectroscopy: principles and techniques

Unique properties of X-rays provide wide range of applications to study the catalytic materials, not only in steady-state environment but also more importantly at in situ and material's operating conditions. Ability to probe metal-site of catalytic material enclosed in gas or liquid environment is possible thanks to penetrating properties of X-rays. In the hard X-ray regime of few keV range, the attenuation length of X-rays is in the order of few thousands of micrometres for low Z materials (like carbon) to few micrometres in lead. Therefore, X-ray spectroscopy provides the depth of probe extensively larger as compared, for example, to electron-based techniques. The second important aspect of X-ray application is the ability to probe both, lowest unoccupied and highest occupied electronic states of an atom. By tuning the X-ray energy close to ionization threshold, the interaction of incidence photon with core-electron leads to electron excitation into unoccupied level above Fermi energy. The fine-tuning of incidence X-ray energy, nowadays easily possible at any synchrotron source, allows thus for precise scanning through the available excitation levels, and as a consequence provides electronic picture of above Fermi electronic states. The photon–electron interaction leading to the creation of the excited intermediate atomic state, decays radiatively to the final state by electron transition from higher electronic level into the created core-hole. This decay channel is accompanied by emission of an X-ray and may be used as probe of occupied electronic states. Therefore, the combination of X-ray absorption process and following X-ray emission event allow for obtaining the complete electronic picture, and hence chemical configuration, of absorbing atom.

In the following, we will discuss the latest developments and trends in X-ray spectroscopy as applied to study catalytic systems, ranging from steady-state measurements to real-time-resolved studies. The combination of X-ray absorption (XAS) and X-ray emission spectroscopies (XES) allowing for resonant X-ray emission spectroscopy (RXES) studies will be presented along with examples of technical developments allowing to extend RXES methodology into the time domain. Finally, the high-energy resolution off-resonant spectroscopy (HEROS) will be described in detail. The advantages and disadvantages of HEROS approach in in situ measurements will be illustrated further on with several practical examples.

### 2.1. Dispersive-type X-ray emission spectrometers

The high-energy resolution resonant and off-resonant X-ray emission spectroscopy relies on measurements of incidence and emission X-ray energies and intensities. In order to obtain meaningful X-ray emission data, the experimental resolution should be of the order of core-hole lifetime of probed atomic species. Typically, the core broadening is in the order of sub-eV up to few eV for K- and L-shells in the X-ray energy range of few keV [7]. The high-energy resolution of incidence X-rays is provided commonly at any synchrotron source by use of double-crystal monochromators. For X-ray detection, dedicated X-ray spectrometers are being developed, with different spectrometer geometries and arrangements depending on particular needs and goals of experiments. In the present section we focus solely on dispersive-type spectrometer because of its particular parameters and operating characteristics.

In comparison to other spectrometer solutions employed at synchrotron beamlines [5, 8] that use two-dimensional focusing, the dispersive-type spectrometer employs only one-dimensional focusing of X-rays. Dispersive-spectrometers are characterized by lower detection efficiency in comparison to, for example, spectrometers working in Johann geometry. On the other hand, the dispersive-spectrometer geometry allows for measurements of X-ray emission spectra in dispersive-mode, which enables detection of X-ray emission in a wide range of energies (few tens to few hundreds of eV) without any scanning elements during measurement. For the experiments requesting short acquisition times, the dispersive-spectrometer geometry may be thus regarded as optimal solution.

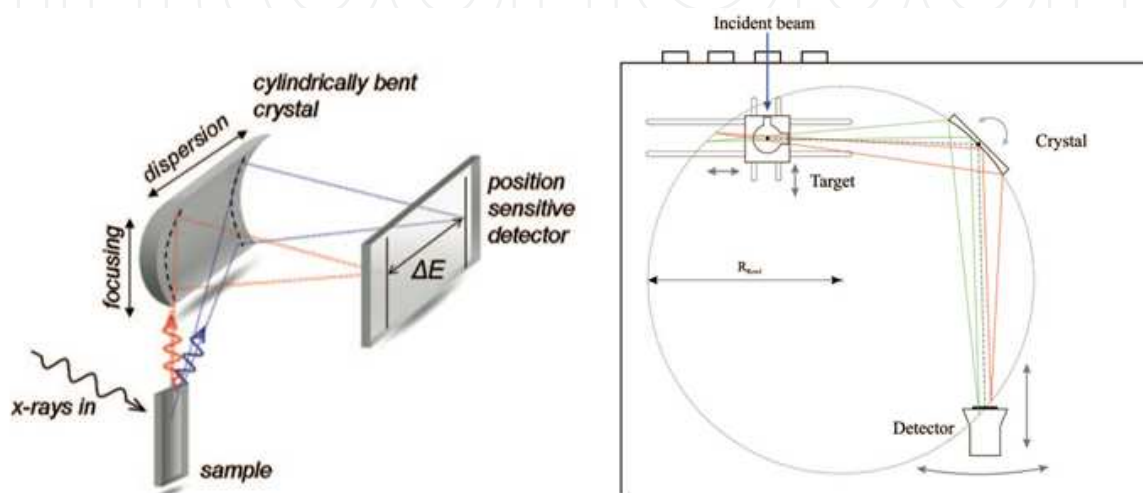


**Figure 1.** (Left) Schematic representation of von Hamos spectrometer geometry (Reprinted with permission from [4]. Copyright (2012), American Institute of Physics). (Right) Schematic view of the geometrical setup used in Johannson geometry (Reprinted with permission from [9]. Copyright (2012), American Institute of Physics)

There are two common geometries allowing for spectrometer setup in dispersive mode: Johannson-type [10] and von Hamos-type [11]. Schematic representation of von Hamos geometry is shown in Figure 1 (left) [4]. In such arrangement, the X-ray fluorescence from the sample is dispersed on cylindrically bent crystal. The dispersion axis and therefore energy range covered by the setup is limited by the length of the crystal/detector along dispersion axis. One-dimensional bending of the crystal aims at increasing the efficiency of the setup, as compared to flat crystal geometry, by focusing the diffracted X-rays onto the detector plane. The von Hamos setup provides good energy resolution being often below 1eV at relatively large Bragg angles. The Bragg angle domain is changed by linear displacement of the crystal and detector along dispersion axis, where the detector distance from the sample is always twice that of the crystal. Because of linear motions of the crystal/detector, the von Hamos spectrometer allows for flexible arrangements around the sample environment. Moreover, because of application of short curvature radii without loss on energy resolution, the spectrometer requires relatively small space for operation. Finally, the spectrometer geometry can be easily extended into multicrystal operation allowing for enhanced spectrometer efficiency or measurements of multiple X-ray emission lines [12].

In Johannson geometry, schematically shown in Figure 1 (right), the X-ray fluorescence from the sample is diffracted by cylindrically bent crystal; however, unlike in von Hamos geometry,



the crystal curvature is positioned in dispersive axis. For Johannson geometry, the Bragg angle planes are not parallel to the crystal surface and therefore the energy broadening at lower Bragg angles is eliminated. Thanks to this, a wider Bragg angle range may be applied at high-energy resolution of the spectrometer. As a consequence, only few diffraction crystals are necessary to operate the spectrometer over broad energy range. By operating the Johannson spectrometer in the off-Rowland geometry the X-ray emission spectrum over certain bandwidth is measured, which is given by the detector length along dispersion axis. The drawback of off-Rowland setup is that only small part of the crystal contributes to the X-ray diffraction at one energy channel; however, this efficiency loss is somehow compensated by recording entire X-ray emission spectrum without scanning components.

Both spectrometers, von Hamos and Johannson types, yield absolute energy resolution significantly below the lifetime of characteristic emission lines, being crucial for detailed analysis of spectral features. The provided dispersive type of detection can be exploited to record time-resolved off-resonant, resonant and nonresonant X-ray emission studies. Because of ability of performing quick acquisitions of X-ray emission spectra, the spectrometers may be applied for in-situ spectroscopic studies of dynamic systems.

## 2.2. $K\beta$ and valence-to-core RXES

The method of resonant emission X-ray scattering (RXES) is recognized as one of the most sensitive measurement techniques that allows the detection of very small changes in the electronic structure of studied element [13]. The method is based on X-ray scattering process in which the core electron is excited to unoccupied electronic states above Fermi level, and simultaneous detection of X-ray emission accompanied by atomic decay from intermediate to final state. By the monitoring of X-ray intensity and X-ray emission shape analysis, the detailed information on the electronic structure may be retrieved.

As an example, in Figure 2 we show the  $K\beta$ -RXES plane for  $\text{TiO}_2$  anatase recorded around Ti K-absorption edge [18,21]. In the experiment, the incidence X-ray energy was tuned around 4968–4992 eV range allowing probing by 1s electron the lowest unoccupied electronic states. Simultaneously, the  $K\beta$  and valence-to-core decay channels were measured by means of dispersive-type von Hamos spectrometer. The relatively large range of spectrometer crystal along dispersive axis, allowed to probe both  $K\beta$  and valence-to-core transition at once, so that only the incident beam energy had to be scanned to record the full RXES plane.

The measured RXES map exhibits several features depending on excitation and emission X-ray energy. The first X-ray emission signal appears at incidence X-ray energy of around 4968 eV. This weak pre-edge feature corresponds to the 1s-3d-like excitation and extends up to the excitation energy of 4974 eV. The s→d types of electron excitations are quadrupole transitions that are characterized by relatively small excitation probability as compared to dipole excitations, which are commonly examined by RXES. However, as shown with the help of theoretical calculations, because of the strong d→p hybridization in  $\text{TiO}_2$  compound, the 1s→3d excitation is characterized by a relatively high excitation probability. RXES measurements using transitions from higher electronic states (i.e., 3p→1s) proved to be extremely sensitive to determine the nature of the lowest unoccupied 3d states of Ti. With the excitation of an electron from a

1s shell to a 3d-localized state, excited electron interacts with the 3p electron, resulting in a shift of 3p→1s emission line by 1.8 eV to lower energies due to the electron–electron interaction effect. This effect can be seen in RXES plane in Figure J1 for lowest excitation energy of 4968 eV. However, if the 3d excitation state is delocalized, the electron–electron interaction is negligible and shift of 3p→1s emission is thus not observed for pre-edge features at excitation energies above 4970 eV. The K $\beta$  and valence-to-core RXES measurements give unique opportunity to investigate simultaneously lowest unoccupied and highest occupied electronic states by X-ray absorption and X-ray emission spectral projections (see for details [18, 21]). We shall discuss shortly here the possibility of determining the absolute value of the energy band gap as well as possibility to employ RIXS measurements in cases where the commonly used optical methods are insufficient (i.e., in the case of “dark-samples” or samples containing so-called color-centers). The results obtained to date suggest that determination of the absolute band gap energy by K $\beta$ -RIXS may be difficult due to interactions of the core excited electron with 3d valence electrons as well as because of the effects of core-hole shielding. Both processes can induce a small, but not negligible, change to the electron levels before Ti atom decays to its final state. However, the obtained K $\beta$ -RIXS results based on comparison experimental RXES spectra of rutile and anatase TiO<sub>2</sub> structures suggest that the relative change in the band gap energy can be determined and examined to a high precision.

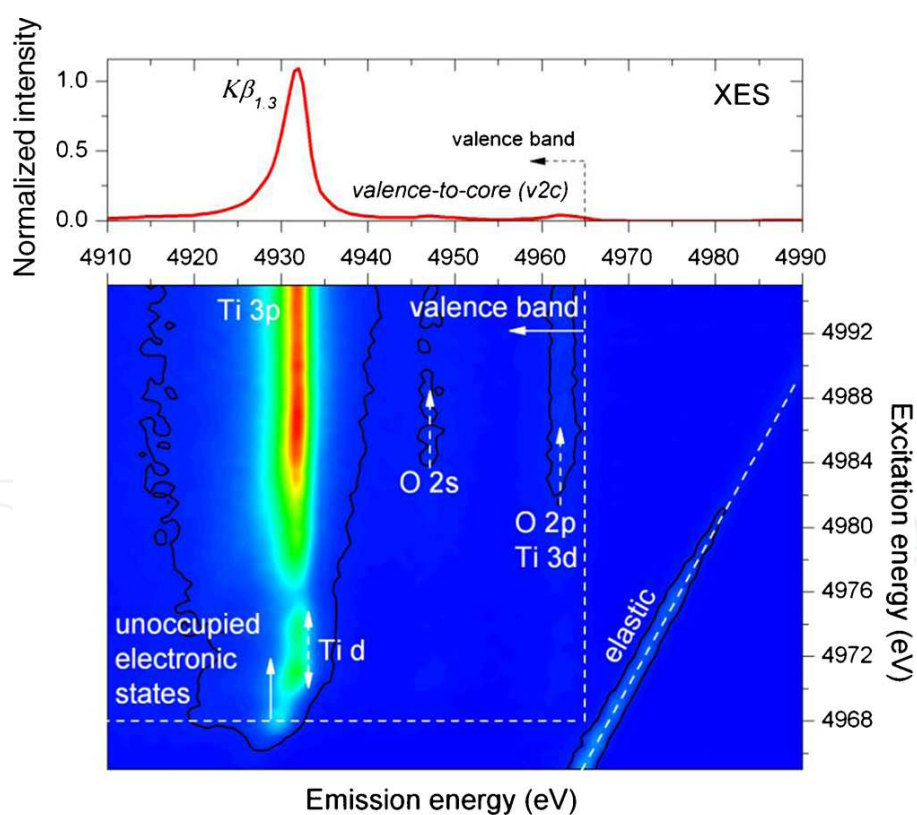


**Figure 2.** K $\beta$ -RXES plane of TiO<sub>2</sub> anatase measured for Ti around K-absorption edge. The main detected spectroscopic features are labeled on the RXES plane. On top, the nonresonant K $\beta$  and valence-to-core X-ray emission spectrum is shown, which was recorded for incidence X-ray energies above K-shell ionization threshold. (From [18] - Reproduced by permission of The Royal Society of Chemistry)

### 2.3. Time-resolved RXES

The use of X-ray spectroscopic methods for measuring a high time resolution data is limited by several technical factors. RXES measurements, employing two-dimensional focusing crystals, requires scanning of both incidence and emission X-ray energy. Therefore, the RXES method, despite the exceptional sensitivity of the measurement, could be applied only in experiments in which the sample was kept in a steady-state chemical equilibrium. The use of dispersive-type spectrometer for RXES spectroscopy significantly reduces the measurement time due to the dispersive type of detection of X-rays emitted from the sample. In such experimental configuration, the measurement time is determined only by the speed of the scanning incidence X-ray beam energy, which at present synchrotrons may be in the order of a several seconds [42, 43]. The acquisition time is an important aspect in the study of irreversible processes in which repeating the experiment at the same chemical conditions is very difficult or sometimes even impossible, for example, because of the small amount of available sample.

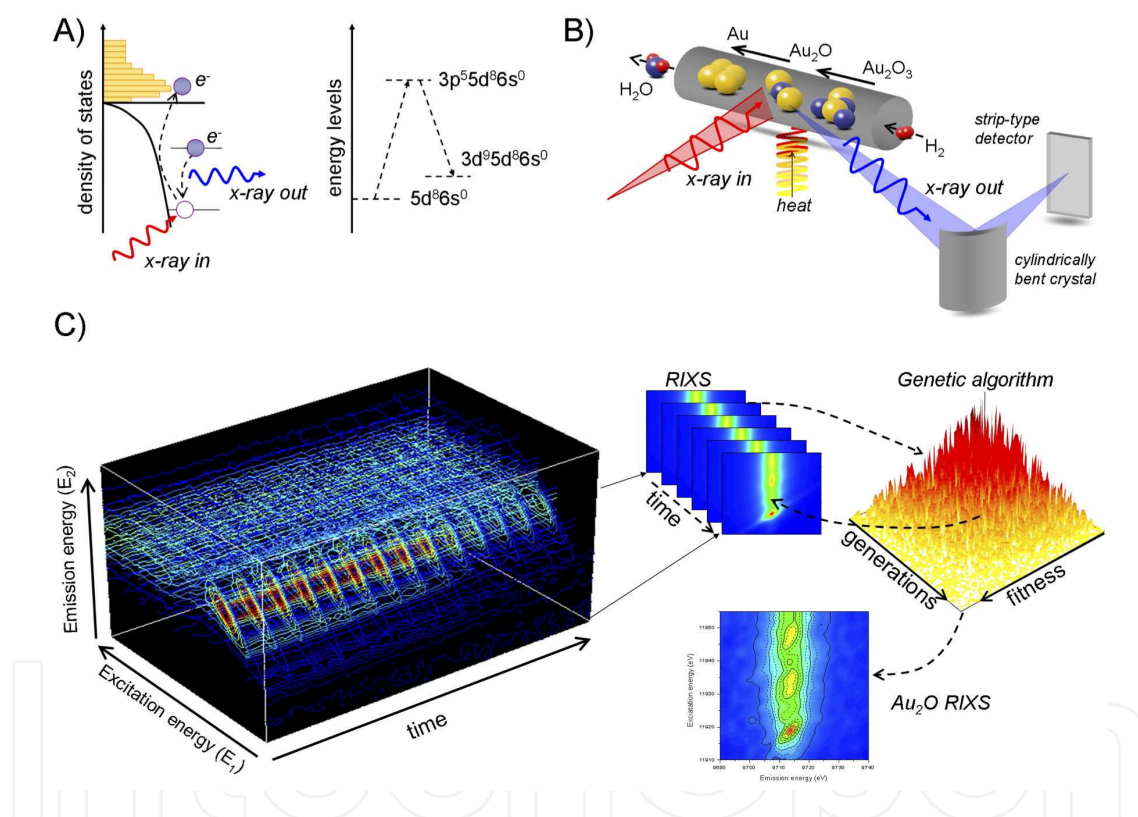


**Figure 3.** a) Scheme showing RXES process in gold. b) Experimental setup employed for in situ RXES spectroscopy. c) Series of RXES planes measured during the experiment (time-resolved RXES) together with schematic description of data analysis using genetic algorithm. (Reprinted with permission from [43] Copyright (2014) American Chemical Society)

As an example, we briefly discuss the aspect of time resolution in RIXS measurements by employing dispersive spectrometer to study the local electronic structure of Au in the temperature-programmed reduction (TPR) of Au<sub>2</sub>O<sub>3</sub> gold oxide. During the measurements, the gold oxide Au<sub>2</sub>O<sub>3</sub> was maintained under H<sub>2</sub> atmosphere and at the same time heated continuously at a rate of about 5°C per minute in the range from 20°C to 300°C. Schematic description of the experimental setup is shown in Figure 3, together with evolution of experimental time-



resolved RXES spectra. RXES experiment, employing excitation from  $2p_{3/2}$  to  $5d$  and following decay transition from  $3d_{3/2}$  to  $2p_{3/2}$  final state, showed a change in electronic valence configuration of Au from  $5d^86s^0$  to  $5d^{10}6s^1$ , corresponding to gold oxide  $Au_2O_3$  reduction to the metallic form  $Au^0$  at temperatures above  $150^\circ\text{C}$ . However, as stressed in [43], thanks to obtained time resolution of RXES acquisition, the transitional forms of Au in the configuration of  $5d^{10}6s^0$  and corresponding to the formation of gold (I) oxide (i.e.,  $Au_2O$ ) were registered. The result was surprising, because the  $Au_2O$  compound is unstable and is quickly reducing to a form of  $Au^0$ . On the basis of RIXS measurements and by using analysis based on genetic algorithm, it was possible to determine the structure of  $5d$  electronic states, as well as to determine the  $Au_2O$  crystallographic structure. The experimental results were examined with density functional theory (DFT) calculations, confirming the two-stage reduction process of  $Au_2O_3$ . The application of the RXES technique with high temporal resolution has been the key to obtain the described results. The time-resolved RXES enabled for the first time to investigate the structure of the unstable gold (I) oxide.

## 2.4. High energy resolution off-resonant spectroscopy

In many synchrotron studies of chemical processes the experiments are artificially slowed down in order to obtain good quality experimental data. The time limit, of the order of several seconds, drawn by the need of scanning the incident X-ray energy, was still a major constraint to study the electronic state of matter under working conditions as well as main restriction in ability to follow individual reaction steps. The idea for solving these technical problems was the application of off-resonant X-ray scattering, a process of photon-atom interaction for excitation energies being set below an absorption threshold [14]. The concept of using off-resonant X-ray scattering process dates back to 1982, when based on the Kramers-Heisenberg theory, J. Tulkki and T. Åberg developed simplified differential equations describing the interaction of photons with the atom [15]. In this theoretical study they found that for the incidence X-ray beam energy tuned below the absorption edge of an atom, the shape of the X-ray emission spectrum (XES) is proportional to the density of unoccupied electronic states, i.e., equivalent to X-ray absorption. However, the potential and possibilities of determining the electronic structure from the X-ray emission spectra at off-resonant conditions has not been extensively studied due to its very low cross section.

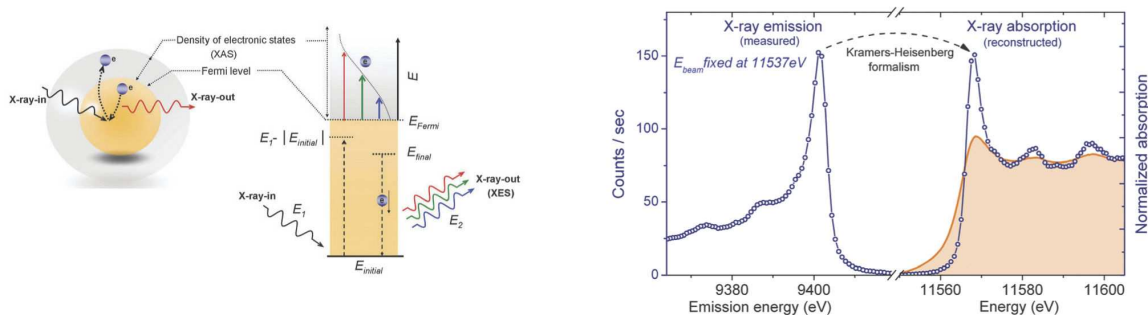


**Figure 4.** Schematic representation and energy level drawing for an off-resonant scattering process (left). On right we plot HEROS-XES for the  $3d_{5/2}-2p_{3/2}$  transition of a Pt foil recorded at excitation energy of 11537 eV. The reconstructed HEROS-XAS spectrum using Kramers-Heisenberg formalism is also plotted and compared to conventional total fluorescence yield XAS. (Adapted from [61] - Reproduced by permission of The Royal Society of Chemistry)

Correspondence of off-resonant scattering and X-ray absorption processes can be derived starting with simplified cross-section formulas describing photon–atom interaction in vicinity of ionization threshold. Within the Kramers-Heisenberg approach, the differential cross sections for resonant X-ray scattering can be expressed as follows [15] (Eq. 1):

$$\frac{d\sigma(\omega_1)}{d\omega_2} = 2\pi r_0^2 \int \frac{\omega_2}{\omega_1} \frac{(\omega_i - \omega_f) g_{fi} (\omega_i - \omega) dg_i}{d\omega} \frac{\frac{\Gamma_f}{2\hbar}}{(\omega_i + \omega - \omega_1)^2 + \frac{\Gamma_i^2}{4\hbar^2}} \frac{\frac{\Gamma_f^2}{4\hbar^2}}{(\omega_1 - \omega_f - \omega - \omega_2) + \frac{\Gamma_f^2}{4\hbar^2}} d\omega$$

where  $r_0^2$  is the classical electron radius. The energies of the initial and final states are represented by  $\hbar\omega_i$  and  $\hbar\omega_f$ , whereas  $\hbar\omega_1$  and  $\hbar\omega_2$  are the incoming and outgoing photon energies, respectively. The initial and final state broadenings are given by  $\Gamma_i$  and  $\Gamma_f$ . The  $g_{fi}$  stands for the oscillator strength of the X-ray transition from the final to initial vacancy state, and the  $dg_i/d\omega$  represents the oscillator strength distribution for electron excitation.

The second term in Eq. 1 ensures the energy conservation given by  $\omega = \omega_1 - \omega_f - \omega_2$  and accounts for the final state broadening ( $\Gamma_f$ ). By neglecting the final state width, the second term of Eq. 1 can be replaced by the Dirac delta function (Eq. 2):

$$\frac{d\sigma(\omega_1)}{d\omega_2} = 2\pi r_0^2 \int \frac{\omega_2}{\omega_1} \frac{(\omega_i - \omega_f) g_{fi} (\omega_i - \omega) dg_i / d\omega}{(\omega_i + \omega - \omega_1)^2 + \Gamma_i^2 / 4\hbar^2} \delta(\omega_1 - \omega_f - \omega - \omega_2) d\omega$$

For the off-resonant excitations the oscillator strength distribution ( $dg_i/d\omega$ ) is directly proportional to the X-ray absorption spectrum (XAS). Therefore, the shape of the X-ray emission spectrum (XES), which is proportional to the differential cross sections, can be described as follows (Eq. 3):

$$XES(E_2) = \int \frac{E_2}{E_1} \frac{(E_i - E_f)(E_i - E) XAS(E)}{(E_i + E - E_1)^2 + \Gamma_i^2 / 4} \delta(E_1 - E_f - E - E_2) dE$$

the above equation the constants were omitted and frequencies replaced by E according to  $\omega = E/\hbar$ . By keeping  $E_1 - E_f - E - E_2 = 0$ , Eq. 3 can be represented analytically for XAS(E) solution (Eq. 4):

$$XAS(E) = \frac{E_1}{E_2} \frac{(E_i - E_f - E_2)^2 + \Gamma_i^2 / 4}{(E_i - E_f)(E_i - E_f + E_1 - E_2)} XES(E_2)$$

This simplified formula provides the XAS(E) function that can be analytically solved for any measured XES( $E_2$ ). We should note that Eq. 4 is valid only at condition where  $E_1 \ll E_i$ , i.e., the measured off-resonant spectrum is free of any resonant features. Typically, the detuning of excitation energy should be as large as  $5 \times \Gamma_i$ . The final state broadening ( $\Gamma_f$ ), the incoming beam

energy distribution, and the resolution of the X-ray spectrometer are not considered in this equation. Therefore, the derived HEROS-XAS curves will be broadened by these three contributions.

By combining the aspects of off-resonant scattering, high energy and dispersion-type of detection to the measurements of unoccupied electronic states a high energy resolution off-resonant spectroscopy has been established. The proposed method does not require any scanning optical elements during the measurement, and therefore allows for X-ray spectroscopy measurements at timescales unattainable to XAS or RXES techniques [61, 64, 65, 16]. Figure 4 demonstrates the principle of HEROS. The  $L\alpha_1$  X-ray emission ( $3d_{5/2} - 2p_{3/2}$  transition) of a Pt foil was recorded at a fixed incident X-ray beam energy tuned below the L3 absorption edge. The off-resonant X-ray emission was recorded by means of von Hamos spectrometer that allowed to cover over 60eV energy range at fixed optical arrangement. The corresponding HEROS-XAS spectrum was reconstructed using the measured X-ray emission spectrum and Eqs. 1–4. The HEROS-XAS spectrum (open circles) is compared to the X-ray absorption spectrum (filled orange area) that was recorded by means of total fluorescence yield (TFY). We should stress here, that the derived HEROS-XAS spectrum exhibited more detailed information than the conventional XAS spectrum, due to the removal of the initial state broadening. The result implies that the HEROS-XES exhibits the same information as high-energy resolution XAS. Moreover, the HEROS experiment is performed at a fixed optical arrangement, meaning acquisition time resolution is simply controlled by experimental efficiency, not by the speed of scanning the incident energy axis. Finally, as recently demonstrated, the HEROS spectra are free of self-absorption effects [63]. Self-absorption belongs to one of the phenomena disturbing the absorption measurements [17] and leads to a modification of the shape of the measured absorption spectrum, visible in particular in the case of samples having high concentrations of the studied element. There are several methods, both computational and experimental, that allow minimizing the effects of self-absorption in the experimental spectra, but until now there was no spectroscopic method allowing direct measurement of the XAS spectra that does not contain the effect of self-absorption. No effect of self-absorption in the HEROS measurement is explained by a fixed experimental geometry (i.e., no scanning optical elements during measurements), allowing for the acquisition of spectra at fixed both incident beam and emission energies. Therefore, the HEROS method could be used not only for measurements requiring a high time resolution, but also in the experiments, where the exact knowledge of the electronic structure is essential for the chemical speciation or theoretical calculations.

### 3. Case studies

#### 3.1. Materials' characterization

Photocatalytic properties are intimately related to the electronic structure of the employed semiconductors. They determine materials' optical properties and to a large extent surface reactivity. RXES measurements can determine the electronic structure of conduction band

(XAS) and valence band (v2c-XES). To demonstrate RXES abilities, we determined the electronic structure of N-doped  $\text{TiO}_2$  [18].  $\text{TiO}_2$  is the most used photocatalyst, and N-doping is often used to change its band gap in order for the material to absorb in the visible range.

In the case of photocatalysts, and more specifically on N-doped  $\text{TiO}_2$ , the fundamental aspects for a high-performing material are: decent overlap between N and O orbitals (synergy effect), and dense and wide orbital levels in the conduction band (charge mobility). The first aspect defines how well-mixed the doped system is, a key parameter toward achieving the desired synergetic effect and visible light absorption. In the worst case scenario, the resultant material is composed of a solid solution of two different materials, namely,  $\text{TiO}_2$  and  $\text{TiN}$ . The second aspect refers to charge mobility, which in the case of  $\text{TiO}_2$  like any other semiconductor occurs via charge particles carriers trapping and detrapping mechanism [19]. Therefore, charge mobility depends on the number of available orbital levels (sub-bands) in the conduction and valence band and spacing between them.

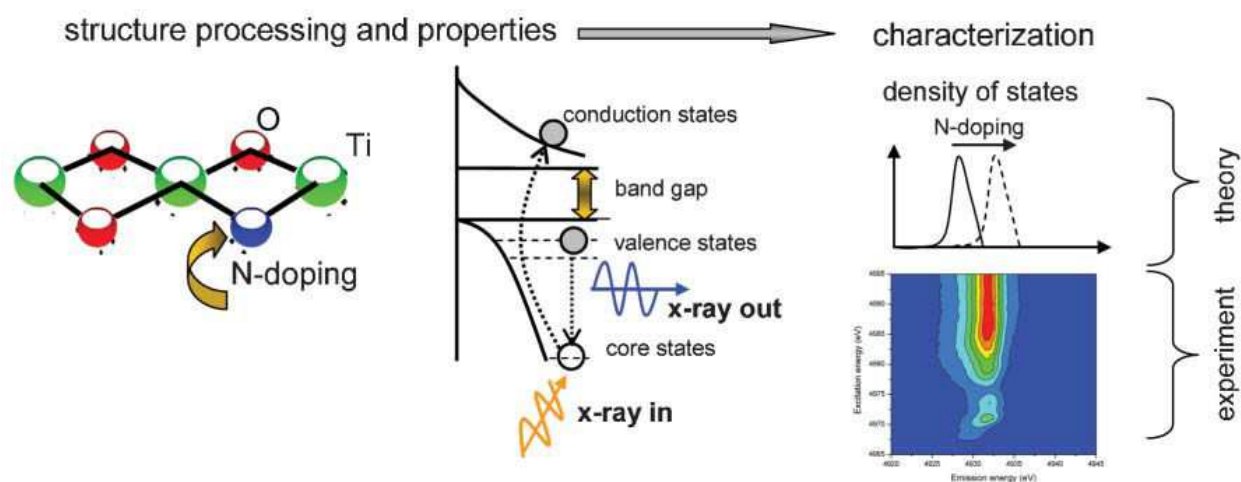


**Figure 5.** Schematic representation of combined theory and experimental approach for the design of improved doped semiconductors. (Reproduced from elsewhere [18] with permission)

By combining RXES measured at Ti K-edge and FEFF calculations [20], we were able to determine the electronic structure of conduction band (XAS) and valence band (valence-to-core X-ray emission spectroscopy (v2c-XES). Figure 5 represents schematically the procedure to attain information about semiconductor electronic structure.

Figure 6 shows the effect of substitutional N-doping of  $\text{TiO}_2$ . Starting with pristine  $\text{TiO}_2$ , the XAS (conduction band) is constituted primarily of Ti-d empty states. The two peaks in the spectrum relates to the octahedral crystal field separation of the d-orbitals. The lowest energy peak is associated to the  $t_{2g}$  orbitals and the highest to  $e_g$  orbitals. The valence band (v2c-XES) is composed of O-2p and occupied Ti-d states. The valence edge is composed entirely of oxygen orbitals. However, the states are well-hybridized, thus one cannot state that electrons excited from valence edge are from oxygen. Rather, one can state that they were located in the oxygen orbitals at the time of the excitation.

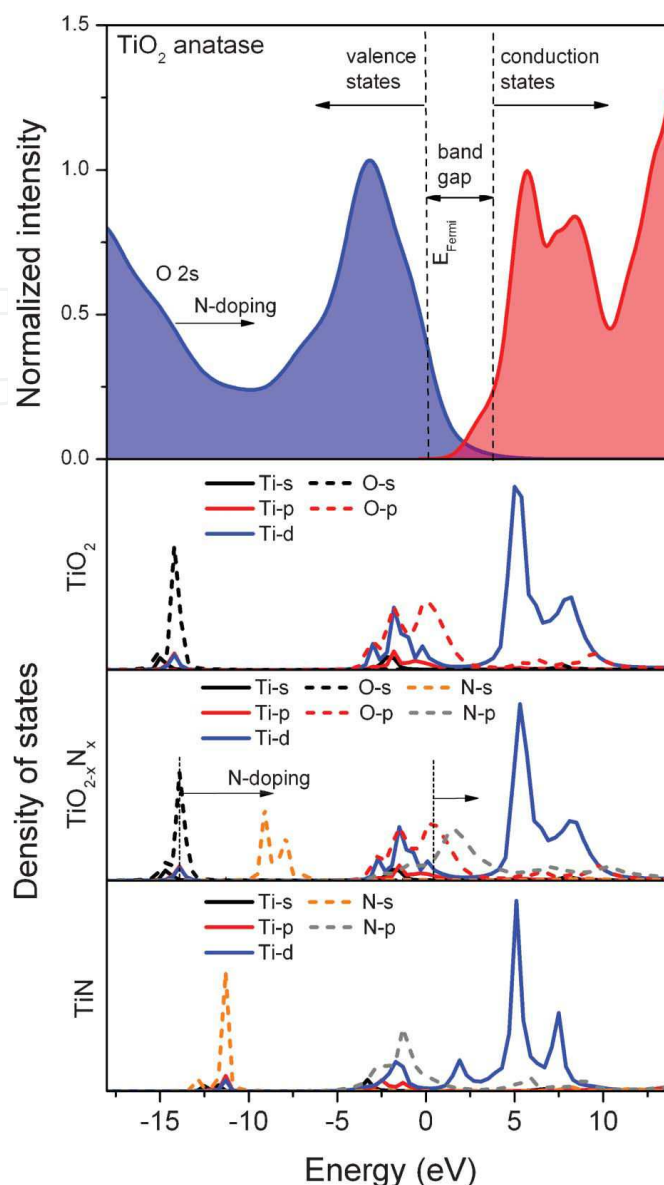


**Figure 6.** Electronic band structure of TiO<sub>2</sub> and TiN. (Top) Valence and conduction band electronic states extracted from measured RIXS plane. (Below) Calculated Ti, O, and N DOS for TiO<sub>2</sub>, TiN, and TiO<sub>2-x</sub>N<sub>x</sub>, where x amounts to 2% N-dopant level. (Reproduced from elsewhere [18] with permission)

The addition of N led to a shift of the valence edge to higher energy, i.e., reduction of semiconductor band gap. The shift is due to the appearance of N-2p orbitals that are strongly hybridized with O-2p orbitals. However, too much N-doping results in the formation of TiN and consequent coloring in the sample, but according to the electronics of the materials, TiN could not work as a sensitizer. Plus, it is known that TiN has no catalytic activity and thus might decrease activity by blocking and/or reducing surface sites.

By confirming RXES measurements with FEFF calculations, we derived an elegant and cost-effective strategy for the rational design of novel materials used in the conversion of solar energy into chemical bonds. Together, one is able to map the material electronic structure with



high precision, requiring a very limited amount of sample (experimental work) or none (theory). The technique can be applied to other materials in all the forms they are normally found, namely nanopowders, and thin-films forms [21].

### 3.2. Molecular adsorption

Reagents' adsorption is the initial step of any catalytic reaction, and the interaction between reactants and active site is governed by the electronic structure of the catalyst, which determines adsorption strength and geometry [2]. Thus, modification of the active site electronic structure alters reactant adsorption parameters. It is therefore crucial to attain information about adsorption parameters, preferentially under relevant conditions. Surface science studies and theoretical calculations provided over the years a platform to acquire information about these parameters under model conditions, and idealized surfaces. However, this valuable information is difficult to correlate with reactions carried out in liquid phase and/or pressure.

Catalytic hydrogenations with molecular  $H_2$  are unquestionably the workhorse of catalytic organic synthesis. The synthetic capacity of catalytic hydrogenation is superbly condensed in Rylander's following quotation [22]: *Catalytic hydrogenation is one of the most useful and versatile tools available to the organic chemist. The scope of the reaction is very broad; most functional groups can be made to undergo reduction, frequently in high yield, to any of several products. Multifunctional molecules can often be reduced selectively at any of several functions. A high degree of stereochemical control is possible with considerable predictability, and products free of contaminating reagents are obtained easily.* Most of the above comments apply to heterogeneous catalytic hydrogenations over supported Group VIII metals [23].

Alternatively to molecular hydrogen, hydrogen donors such as isopropanol or formic acid can be applied in transfer hydrogenations but they generate unwanted side products. Several important inventions have been accomplished in the last 150 years, such as the application of highly dispersed metals, e.g., nickel, in the hydrogenation of organic compounds [24], selective semi-hydrogenation of  $C\equiv C$ -bonds in the presence of Pd-Pb/ $CaCO_3$  catalysts (Lindlar catalyst) [25], and more recently asymmetric hydrogenations [26], pioneered by Knowles and Noyori for which they received in 2001 the Nobel Prize in Chemistry. Catalytic hydrogenations can be carried out in a variety of ways, namely liquid or gas phase, and in batch-wise or continuous mode.

Hydrogenation reactions involving hydrogen dissociation on the metal surface have high reaction probability on many surface sites: top, bridge, and step sites. For this reason, hydrogenation reactions are usually structure-insensitive in respect to hydrogen activation. However, the reaction is considered structure-sensitive in respect to the hydrocarbon hydrogenation. Crespo-Quesada et al. [27] reported that semi-hydrogenation of alkynes occurred preferentially on terraces, whereas further hydrogenation to the alkane occurred at the edges. Similarly, Schmidt et al. [28] revealed that in ethyl pyruvate enantioselective hydrogenation the Pt(111)/Pt(100) ratio controlled reaction rate and enantiomeric excess.

Platinum group metals are highly active hydrogenation catalysts, operating at low temperatures and  $H_2$  pressures. However, their scarcity and high cost intensified the research devoted

in finding alternative catalysts deprived of noble metals. One should be made aware that fine chemical industries, such as the ones responsible for the production of vitamins and fragrance, afford products of medium added value. Accordingly, the use of noble metals and/or sophisticated ligands is only justified when the turnover number is higher than 1000 or even 10,000 depending on the cost of the target product [29]. Nonprecious metal catalysts, especially those based on nickel (e.g., Raney nickel [30], Urushibara nickel [31], CENTOPRIME [32] catalysts) have also been developed as economical alternatives, but they are often less active, requiring higher temperature and  $H_2$  pressure to attain comparable performance.

The chemoselective hydrogenation of  $C=C$  and  $C=O$ -bonds is extensively used in the preparation of pharmaceuticals, fragrances, and vitamins precursors. Common substrates are unsaturated ketones, aldehydes, or esters, which have to be hydrogenated selectively either at the  $C=C$  or  $C=O$  bond depending on their end-use. Palladium and platinum are routinely used to hydrogenate  $C=C$  bonds [33]; however, the systems lose their effectiveness when the molecule contains several hydrogenable functionalities. Chemoselective hydrogenation of unsaturated aldehyde, ketones, and esters has been catalyzed over a plethora of 3d transition metal catalysts [34]. For example, Ni and Cu catalysts were found both active and selective in the hydrogenation of  $C=O$  instead of  $C=C$  [35].

As aforementioned, platinum is routinely used in the chemoselective hydrogenation of  $C=C$  and  $C=O$ -bonds. Recently, Manyar et al. [36] demonstrated that Pt supported on OMS-2 possesses different affinities in the chemoselective hydrogenation of  $C=C$  and  $C=O$ -bonds depending on the substrate used. 5 wt% Pt/OMS-2 (Pt average particle diameter 2 nm) supported on cryptomelane manganese oxide octahedral molecular sieve provides high selectivity for the hydrogenation of both ketoisophorone and cinnamaldehyde. However, in the case of ketoisophorone hydrogenation, 98% of the substrate was hydrogenated to (6R)-2,2,6-trimethylcyclohexane-1,4-dione (levodione) at 100% conversion, i.e., the catalyst selective reduced the  $C=C$  bond. Whereas in the case of cinnamaldehyde, 80% selectivity for the reduction of the  $C=O$  bond forming cinnamyl alcohol at 100% conversion was found using the same catalyst. The observed selectivity in the ketoisophorone hydrogenation contrasts with the expected Pt behavior, which is commonly preferentially to hydrogenate  $C=O$  versus  $C=C$  bonds. The expected selectivity was observed when the reaction was performed over 5 wt% Pt/ $Al_2O_3$  under the same reaction conditions. A possible explanation for the differences is different adsorption geometry/strength of the substrates.

The change in the Pt electronic structure following the adsorption of an  $\alpha$ ,  $\beta$ -unsaturated aldehyde and ketone was followed by in situ HR-XAS in the liquid phase and the adsorption strength calculated with Density Functional Theory (DFT) [37]. Probably one of the most important outcomes of the experiment is that adsorption of a molecule on Pt surface led to an immediate change in XAS single, i.e., Pt electronic structure. The perceptual change relates to molecule coverage, which in this case is below 10% (Fig. 7a). All the molecules produced a Fermi level shift to higher energies, which suggests electronic density donation from Pt to the adsorbed molecule. Larger energy shifts equates to stronger interactions, and consequently higher adsorption energy. Thus, from the Fermi energy level shifts measured by Pt  $L_3$ -edge HR-XAS, one might interject that cinnamaldehyde has the strongest interaction with Pt followed by  $H_2$  and then ketoisophorone (Fig. 7a).

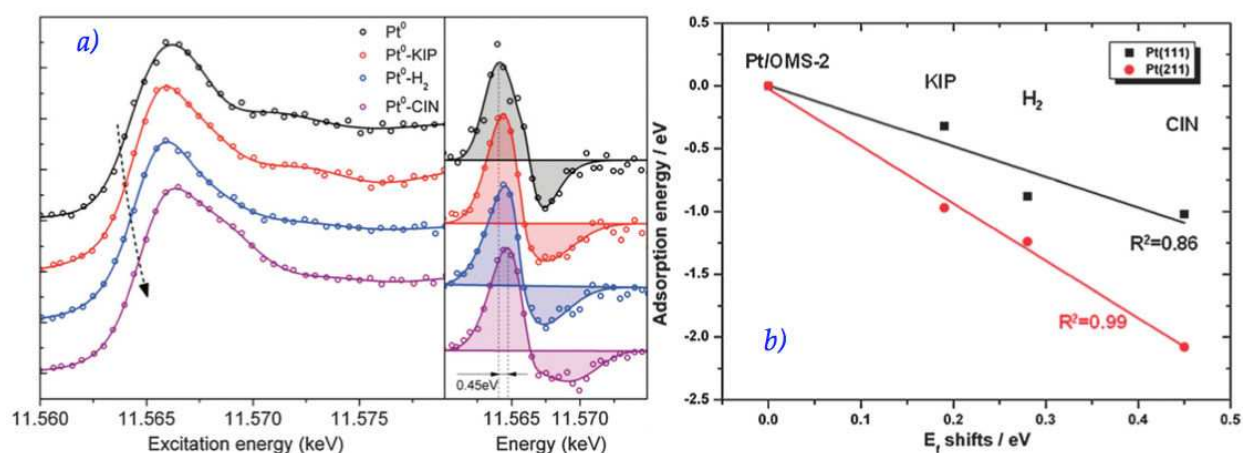


**Figure 7.** (a) Pt L<sub>3</sub>-edge HR-XAS spectra and 1st derivative (right insert) of Pt/OMS-2 interacting with H<sub>2</sub>, KIP (ketoisophorone), and CIN (cinnamaldehyde). The spectra were recorded in situ in 10 mol% methanol in water at 373 K. The lines are from a least squares fitting procedure. (b) Correlation between the experimentally measure shifts in the HR-XAS spectra ( $E_i$ ) and the calculated adsorption energies via DFT for the Pt(111) (black) and Pt(211) (red) surfaces. (Re-produced from elsewhere [37] with permission)

The resulting shift in the Pt Fermi energy, measured at Pt L<sub>3</sub>-edge, due to adsorption of molecules was found to be in good agreement with the molecule adsorption energy trends calculated by DFT, which provided valuable insight into the reaction selectivity (Fig. 7b). It should be mentioned that the experiments were carried out at 373 K and 10 bar pressure, i.e., catalyst working conditions. This was possible due to the development of a homemade cell comprised of a stainless steel autoclave reactor with window comprising of a polyether ether ketone (PEEK) insert [38]. The work confirmed that the combination of state-of-the-art spectroscopy (HR-XAS) and theoretical calculations is a powerful and versatile tool to reveal differences in adsorption behavior for reactants in the liquid phase under reaction conditions, with unprecedented resolution and sensitivity.

Carbon monoxide is often used as chemical probe in spectroscopy because it is very sensitive to the electronic structure of materials. Furthermore, CO is a key reagent in several reactions such as Fischer-Tropsch, PROX, and catalytic converter catalysis. RXES can accurately resolve the occupied and unoccupied d-density-of-states (DOS) of Pt after the adsorption of molecules, including CO [39], under reaction conditions. RXES was found capable of differentiating between the possible adsorption geometries of CO adsorbed on Pt, namely atop, bridged, and faced-bridging [40], making it the ideal tool to determine the changes in adsorption geometry caused by an external effect.

RXES measured at Pt L<sub>3</sub>-edge was used to determine the changes in CO oxidation over platinum sites induced by a magnetic field [41]. CO molecules adsorbed on nonmagnetic Pt nanoparticles supported on a carbon capped Co magnetic nanocore on atop position in the absence of a magnetic field, as expected. Under magnetic field, part of the atop CO changed to the bridged position (Fig. 8), which is a nonreactive state. This result indicates that catalytic activity can be modified by the presence of a magnetic field even if the active site is not magnetic. This opens other potential applications such as molecular displacement on auto-

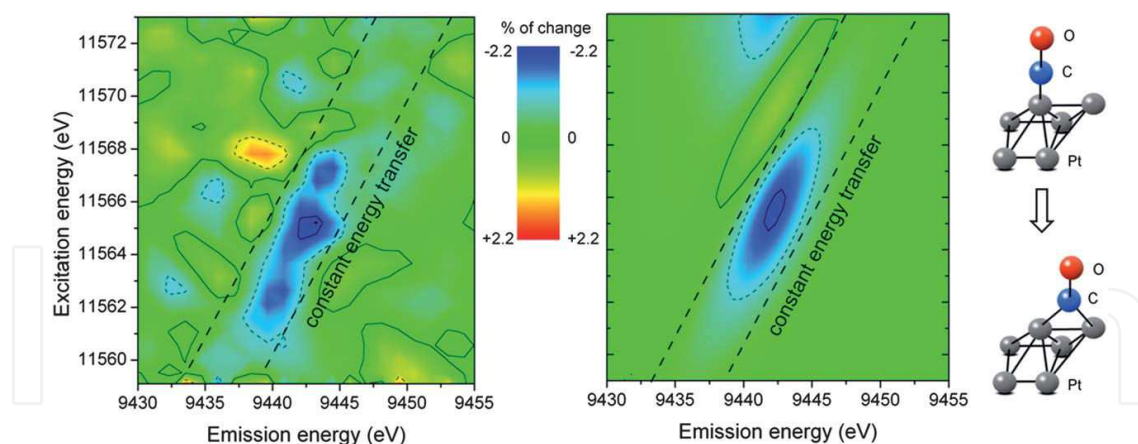


**Figure 8.** Pt  $L_3M_5$   $\Delta$ -RXES due to the presence of a 50 mT magnetic field on Pt on Co with adsorbed CO (field OFF–field ON). (Left) Experimental map differences measured in situ. (Right) Calculated map differences. (Reproduced from elsewhere [41] with permission)

poisoning reactions, characterized by poisoning of reagents, products, and/or trace contaminants that cannot be removed or avoided. For example, hydrogen fuel cells are vulnerable to CO poisoning because CO binds strongly to platinum averting hydrogen adsorption, deterring commercial application. By changing adsorption from atop to bridge, CO adsorption strength decreases by ca. 0.1 eV, enabling its removal at lower temperature.

### 3.3. Study of catalytic reactions under real working conditions (in situ)

Determination of metal oxidation states under relevant working conditions is crucial to understanding catalytic behavior. Temperature-programmed reduction (TPR) is often used to determine the temperature at which the catalyst reduces; however, it fails to determine the oxidation state of the catalyst at this specific temperature. That information is normally attained when a spectroscopic measurement is coupled with the TPR. The reduction behavior of NiO [42] and  $Au_2O_3$  [43] was determined using a novel approach, namely time-resolved RXES or 4D RXES. The experimental concept of such experiment is depicted in Figure 9.

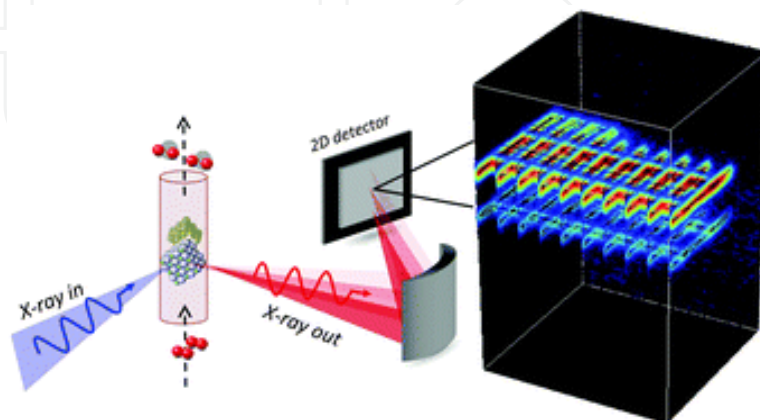


**Figure 9.** Experimental concept for time-resolved RXES measurements. (Reproduced from elsewhere [42] with permission)



Figure 10 shows the RXES map before and after reduction of nano-NiO. A shift in the main signal to lower incidence energies after reduction was observed, coherent with the formation of metallic nickel. From the RXES map one can excerpt information about unoccupied states (XAS analysis) and occupied states (XES analysis). In order to determine reaction pathway, the XAS absorption contribution of NiO and Ni metal was plotted as function of time. The transition from oxide to metallic state was found to be very fast, consisting of single-step reduction mechanism.

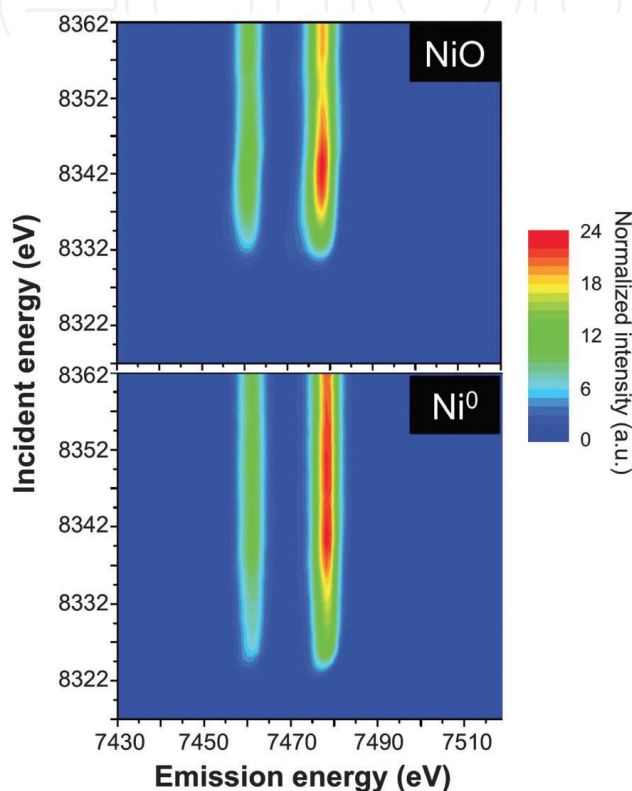


**Figure 10.** RXES map of the initial state (top) and the final state (bottom) of NiO nanoparticle reduction. (Reproduced from elsewhere [42] with permission)

Similar analysis can be performed with XES signals that carry the inherent benefit, when performed in a dispersive-type spectrometer, of high time resolution inaccessible to XAS technique. However, the chemical sensitivity of XES depends on where the analysis is performed. Since this is often unknown a priori, one needs to measure the full RXES map in order to determine the optimal incidence energy to perform XES analysis. The subsequent measurements can be performed only at this range, which decreases drastically the acquisition time, i.e., improved time resolution without losing chemical information. Based on RXES maps, emission analysis above the absorption edge, so-called non-resonant XES or simply XES, is less sensitive to follow the chemical state of atom as compared to resonant XES measured at incoming energies with high discriminating power, in this case at 8325.9 eV (NiO pre-edge) and 8331.9 eV (NiO inflection point) incident beam energy (Fig. 11). This illustrates the importance of knowing at which energy the XES data should be collected.



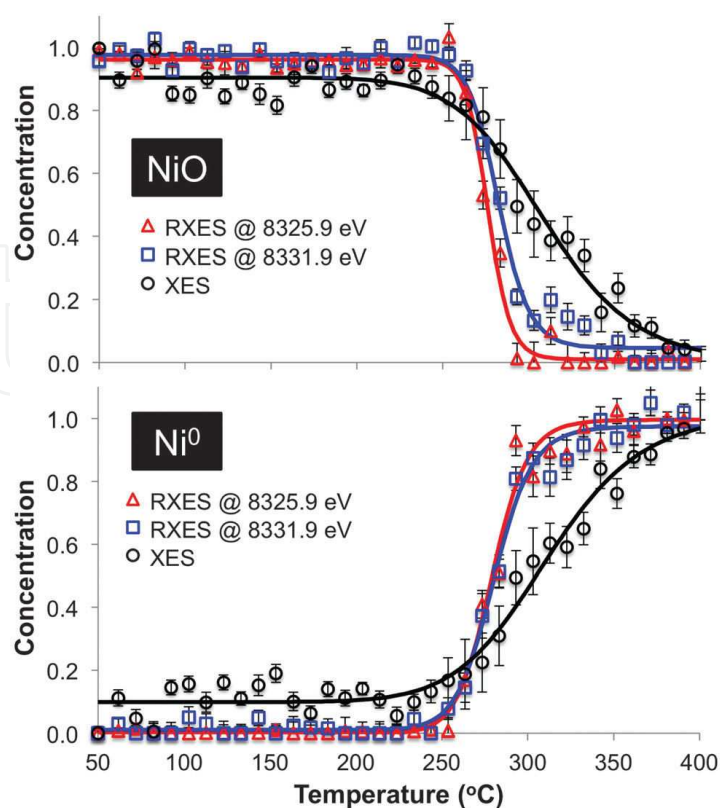


**Figure 11.** Temporal evolution of XES signals for NiO (top) and Ni<sup>0</sup> (bottom) at different incident energies. (Reproduced from elsewhere [42] with permission)

Gold catalysis gained significant popularity after Haruta's discovery that gold nanoparticles are extremely active [44]. Activity of gold is often associated to its metallic phase but some cases consider the involvement of gold in higher oxidations states [45]. The difficulty in detecting gold in oxidations states between 0 and +3 resides in the fact that these intermediate states are unstable and short-lived.

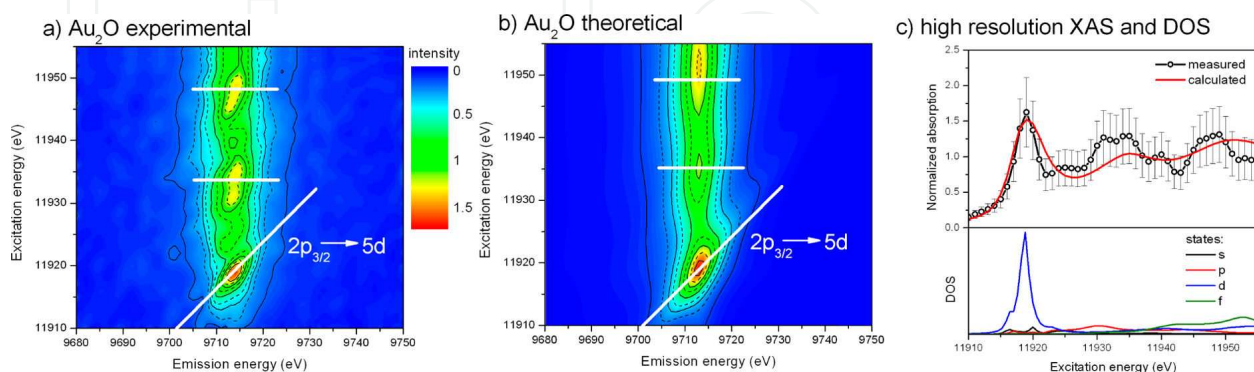


**Figure 12.** (a) Extracted RXES plane of Au<sub>2</sub>O from the time-resolved RXES data set compared to theoretical calculations (b). (c) Assessment between the extracted high-energy resolution X-ray absorption (HR-XAS) spectrum and the matching theoretical predictions. The influence of the DOS of the different orbitals to the X-ray absorption spectrum is plotted in the bottom panel. (Reproduced from elsewhere [46] with permission)

We performed  $\text{Au}_2\text{O}_3$  TPR coupled with time-resolved RXES to see if one could detect some of these intermediate states. A short-lived  $\text{Au}_2\text{O}$  compound was detected for the first time under in situ conditions, permitting a better understanding of the reaction mechanism of  $\text{Au}_2\text{O}_3$  reduction [46]. Based on time-resolved RXES data analysis combined with genetic algorithm methodology, we were able to determine the electronic and geometric structure of the unstable  $\text{Au}_2\text{O}$  transitional specie (Fig. 12). The data analysis revealed a larger value for the lattice constant of the intermediary  $\text{Au}_2\text{O}$  specie as compared to the theoretical predictions. DFT calculations revealed that such structure may indeed be formed, and the expanded lattice constant is justified by the termination of  $\text{Au}_2\text{O}$  on the  $\text{Au}_2\text{O}_3$  structure. The temporal evolution of the species shows the characteristic behavior of a short-lived intermediate state, in this case  $\text{Au}_2\text{O}$  (Fig. 13).

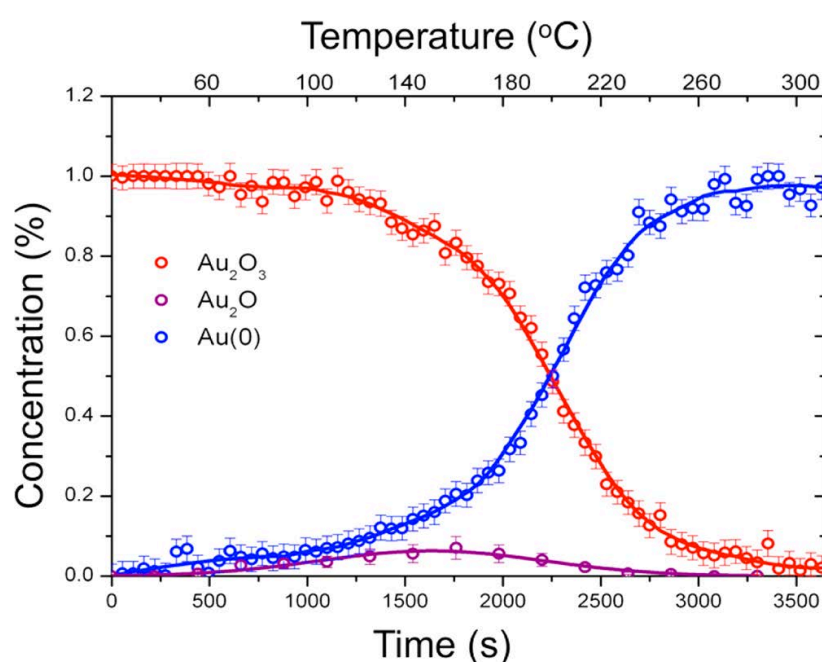


**Figure 13.** Concentration changes of  $\text{Au}_2\text{O}_3$ ,  $\text{Au}_2\text{O}$ , and  $\text{Au}(0)$  during TPR of  $\text{Au}_2\text{O}_3$ . The data are plotted versus time (bottom scale) and temperature (top scale). (Reproduced from elsewhere [46] with permission)

Excessive amounts of oxidants, in particular  $\text{H}_2\text{O}_2$ , can injure proteins and lipids resulting in cell death. Oxidative stress has been connected to a multitude of pathophysiological conditions, such as Alzheimer's and Parkinson's diseases, aging, cancer, genetic damage, and tissue damage in cardiac ischemic/reperfusion injury. In nature, enzymes called catalases conduct the catalytic disproportionation of  $\text{H}_2\text{O}_2$  to water and molecular oxygen.

Nitrogen-containing ligand such as imidazoles, is a class of single-site Mn catalase-like complexes. Imidazoles and their derivatives with strong  $\pi$ -donating ability were found to accelerate  $\text{H}_2\text{O}_2$  disproportionation. The complexes display elevated activity in organic solvents but exceptionally small reactivity or even none in water under physiological pH values. The activity improved when a base was added as a promoter. We reported a novel

manganese (II) complex with a pyridine substitute as a ligand (Fig. 14) [47]. The complex was stable and showed catalase-like activity in neutral aqueous solution.

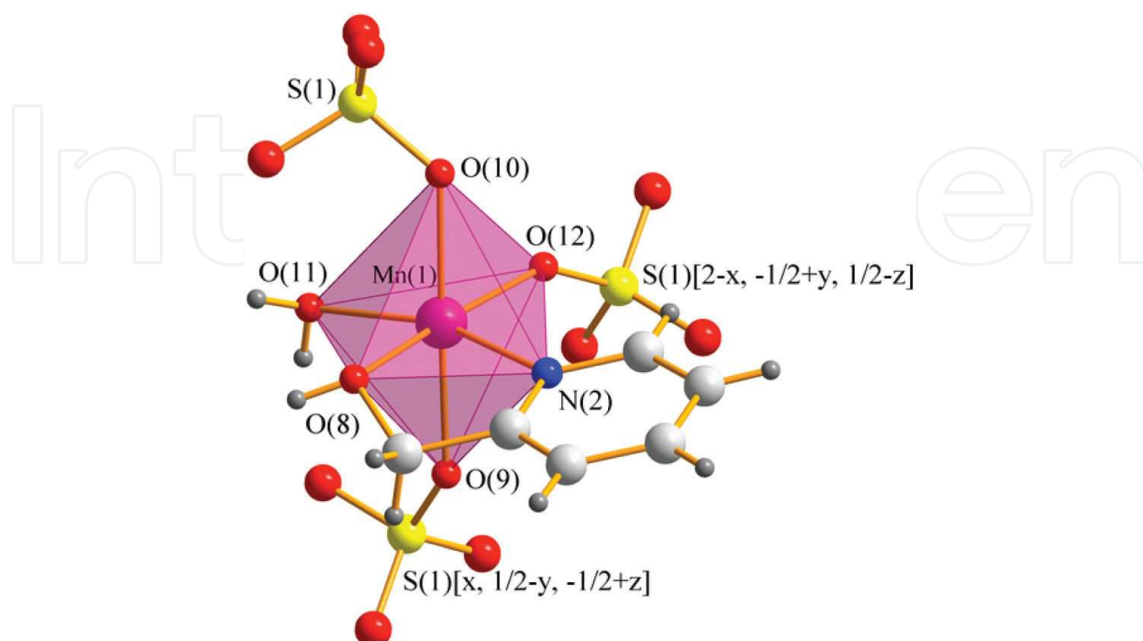


**Figure 14.** DIAMOND diagram showing the coordination environment of Mn(II) in  $[\text{Mn}(2\text{-CH}_2\text{OHpy})(\text{SO}_4)(\text{H}_2\text{O})]_n$ . (Reproduced from elsewhere [47] with permission)

The combination of RXES measured at Mn K-edge and theoretical calculations enables us to propose a reaction mechanism (Fig. 15) in which the manganese complex is firstly oxidized due to the loss of a bridge oxygen proton. This is followed by  $\text{H}_2\text{O}_2$  coordination and proton abstraction by the sulfate group mediated by water. Release of molecular oxygen and catalyst regeneration entails the involvement of a second complex molecule. This affects catalytic reaction rate because they become diffusion-limited. The projected mechanism was the first effort in trying to understand single-site Mn complexes reactivity, and clearly more work needs to be done to establish and understand Mn-catalase mimics' reaction mechanism. Nonetheless, based on findings two novel Mn complexes were synthesized, displaying catalytic activities several orders of magnitude higher than the parent one [48].

The increase in the planet's human population put strong pressure on the food supply chain and energy requirements. Photocatalysis is at the forefront of technologies to produce solar fuels. The first significant breakthrough in converting light into chemical energy was published in 1972 by Fujishima and Honda, who reported the electrochemical photolysis of water assisted by a semiconductor under UV-A radiation [49]. However, despite all the scientific advances, it remains a significant challenge to construct a device capable of producing solar fuels, such as hydrogen, at a scale and cost able to compete with fossil fuels. Moreover, developments based on large band gap semiconductors' ( $>3$  eV), such as  $\text{TiO}_2$ , are hampered by the fact that it requires UV-A irradiation to induce charge separation. Nevertheless,  $\text{TiO}_2$  remains indisputably the best photocatalyst to date [50]. Several efforts are being made to improve sunlight

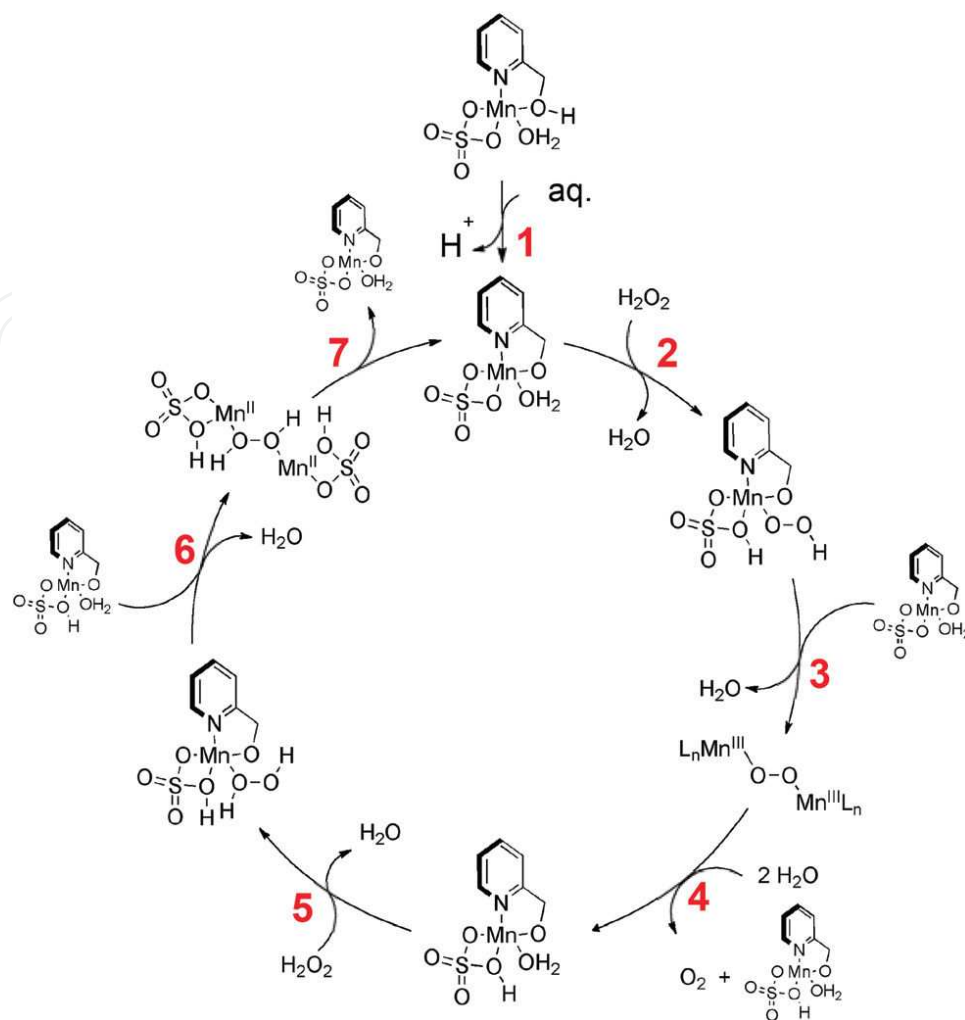


**Figure 15.** Proposed reaction mechanism for  $\text{H}_2\text{O}_2$  disproportionation over  $[\text{Mn}(2\text{-CH}_2\text{OHpy})(\text{SO}_4)(\text{H}_2\text{O})]_n$  in water. (Reproduced from elsewhere [47] with permission)

absorption, including band gap manipulation by doping with elements, such as N, C, and S [51]. However, these are often counterproductive because they decrease the breadth of reactions that can be photocatalyzed and overall performance.

A more promising strategy to circumvent  $\text{TiO}_2$  deficiency in absorbing visible light is to use sensitizers capable of harvesting solar light and introducing hot electrons into the  $\text{TiO}_2$  conduction band (CB). O'Regan and Grätzel [52] developed dye-sensitized solar cells (DSSCs), in which the dye component harvests sunlight and readily injects electrons ( $\tau_{\text{inj}} < 1 \text{ ps}$ ) into the  $\text{TiO}_2$  CB. The success of the dye system depends on fast electron injection and slow back electron transfer. However, organic dyes have low stability, discrete absorption levels (narrow-band), and small optical cross sections, thus requiring a high dye coverage, which diminishes the space available for photocatalytic reactions. Besides, holes in oxidized dyes are unreactive, which hinders hydrogen evolution since a sustainable process demands for equal consumption of electrons and holes.

Metallic nanoparticles (NPs) are interesting sensitizer candidates because of their large optical cross sections related to the excitation of localized surface plasmons (LSP). Gold group metals exhibit plasmonic resonances in the visible region, and their absorption can be easily tuned by changing nanoparticles morphology (shape and size), enabling a good match with the solar spectrum. Moreover, their  $d^{10}$  configuration bestows them chemical stability. Recently, the excitation of Au and Ag LSP nanostructures was shown to improve charge transfer from sensitizer to semiconductor [53], increase the photocurrents under solar irradiation [54], and enhance photoinitiated catalytic oxidations [55]. The latest corroborates that the holes in these structures are reactive and can take part of photo-oxidations.

Hallett-Tapley et al. [56] defended that the plasmon excitation could drive reactions via thermal, electronic, and/or antenna processes. In the case of photocatalysis, the relevant process is the electronic one, in which electrons and holes are allegedly formed upon plasmon excitation [57]. In theory, plasmonic structures can be used directly in photocatalysts; however, the electron-hole pair is short-lived (few femto-second), making it problematic to drive chemical reactions. Interfacial reactions are relatively slow with kinetics in the milliseconds range. To increase charge separation lifetime, the charges can be confined to spatially separated sites where reactions take place. For example, charge separation lifetime can be dramatically improved by coupling LSP structures with a semiconductor (analogous to DSSCs). Mubeen et al. [58] prepared a proof-of-concept system conglomerating the findings on plasmonic nanostructures, water reduction, and oxidation catalysts to produce simultaneously  $H_2$  and  $O_2$  under visible light irradiation. This pioneering work demonstrated system's potential but highlighted the need for improvement.

Despite plasmonic nanostructures' potential, until recently there was no spectroscopic evidence that hot carriers are formed after photon absorption. Since this is essential for the utilization of these structures in photocatalysis, we decided to investigate hot carriers formation on plasmonic structures during illumination. The creation of electron-hole pairs due to LSP excitation was measured by high-resolution X-ray absorption spectroscopy at the Au  $L_3$ -edge, which determines Au 5d unoccupied electronic states. LSP excitation led to an upward shift of the ionization energy threshold by ca. 1.0 eV, and an increase of Au d-band hole population, consistent with hot electrons formation, and their promotion to high-energy states [59] (Fig. 16).

To evaluate if the hot electrons possess sufficient energy to be injected into  $TiO_2$  CB, we carried out transient broadband mid-IR spectroscopy [19]. Free and trapped electrons in a semiconductor conduction band produce a broad mid-IR band. Upon excitation, a broad mid-IR band appeared, confirming the presence of electrons in the  $TiO_2$  CB. The minimum in transmittance was observed at  $t=0$  ps for both systems, which is the best possible overlap between pump and probe pulses, thus confirming fast injection into the  $TiO_2$  and consequently increase in electron lifetime from few fs to 100s of ns. The result corroborates Furube et al. [60] speculated mechanism and more importantly, it indorses that these NPs can drive photocatalytic reactions under solar irradiation.



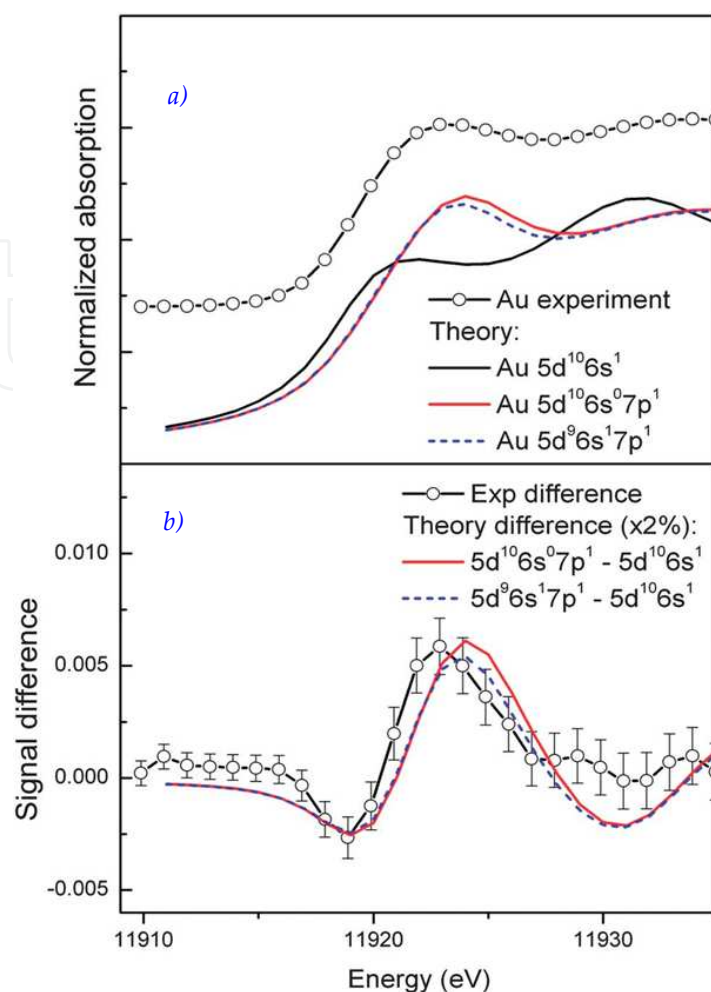


**Figure 16.** HR-XAS experiments portraying variations in the Au DOS induced by continuous wave laser excitation of plasmon resonance at 532 nm, with 100 mW power. (a) HR-XAS ground state spectrum of Au nanoparticles (open circles black trace), FDMNES calculated spectra of the ground state (black trace  $\text{Au } 5d^{10}6s^1$ ) and excited states (red trace  $5d^{10}6s^07p^1$  and blue trace  $5d^96s^17p^1$ ). (b) Difference spectra between the excited and ground state: experimental (open circles black trace), and calculated assuming 2% excitation  $\text{Au } 5d^{10}6s^17p^0 \rightarrow \text{Au } 5d^{10}6s^07p^1$  (red trace);  $\text{Au } 5d^{10}6s^17p^0 \rightarrow \text{Au } 5d^96s^17p^1$  (dashed blue trace). (Reproduced from elsewhere [59] with permission)

We hope that all the arguments mentioned so far demonstrate the capabilities of HR-XAS in understanding catalytic reactivity. However, HR-XAS suffers from an important limitation, namely its time resolution, which is at best of the order of tenths of seconds for ideal samples with high metal concentration. The limitation starts from the fact that HR-XAS measurements entail scanning of the incoming energy, which is restricted to the speed at which the monochromator can be moved. This makes it problematic to monitor a catalytic process in real time. Ideally, the experiments should be carried out in continuous mode in which data collection is carried out synchronously and uninterruptedly, enabling the identification of metastable regimes and intermediate species. HEROS can provide element-specific information about the unoccupied density of states [61], and due to the scanning free arrangement of von Hamos spectrometer, HEROS spectra can be recorded on a shot-to-shot basis with extraordinary time resolution (only depending on sample concentration and photon flux), while upholding

spectral energy resolution [62]. Moreover, HEROS spectra are not perturbed by the self-absorption process [63]. This makes HEROS a commanding tool to identify and quantify the catalyst electronic changes during reaction and as it happens.

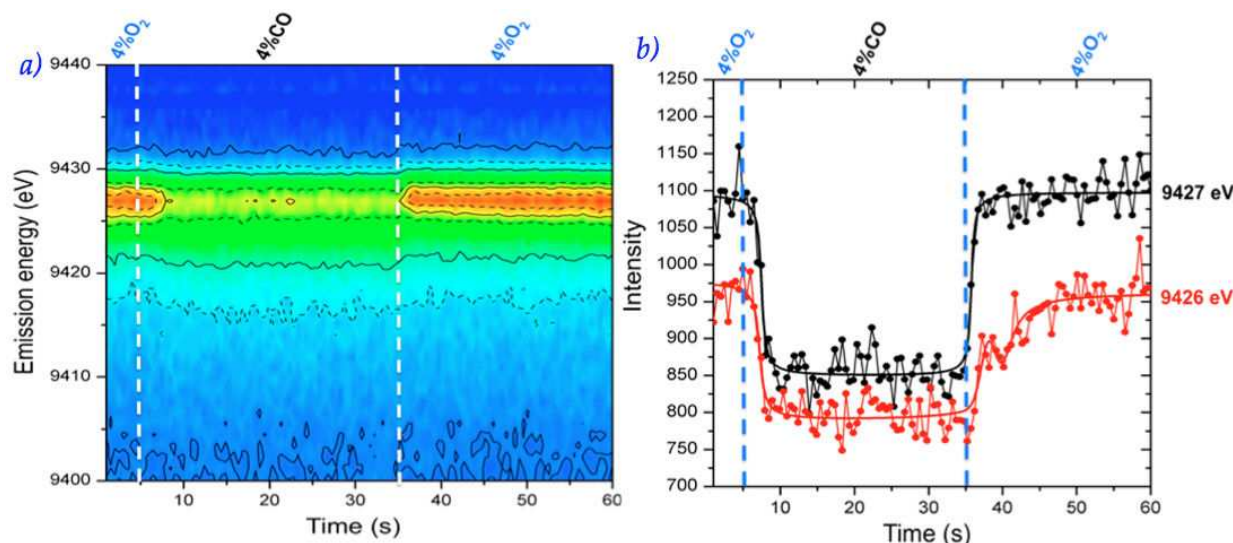


**Figure 17.** (a) Temporal evolution of the HEROS spectra during CO/O<sub>2</sub> switches at 300 °C on 1.3 wt% Pt/Al<sub>2</sub>O<sub>3</sub>. (b) Temporal evolution of the HEROS signals at 9426 and 9427 eV (whiteline region) during CO/O<sub>2</sub> switches. (Reproduced from elsewhere [64] with permission)

We performed an in situ time-resolved HEROS study with subsecond resolution providing insight into the oxidation and reduction steps of a Pt catalyst during CO oxidation with 500 ms resolution [64]. Figure 17 displays a gentle oxidation step, comprised of two distinguishing stages, namely dissociative adsorption of oxygen followed by partial oxidation of Pt subsurface. By comparing the experimental spectra with theoretical calculations, we found that the intermediate chemisorbed O on Pt is adsorbed on atop position, insinuating CO surface poisoning or surface reconstruction. This indicates HEROS ability to perform chemical speciation with subsecond time resolution, which opens exciting opportunities to follow catalysis in real time. Since the HEROS spectra are collected in a single shot, the time resolution can be further improved since it depends only on the number of incoming photons and element concentration, which makes it particularly suited for experiments at the XFELs. Recently, it was shown that experiments with 100 ms resolution could be achieved at the synchrotron [65].

#### 4. Outlook and future trends in the field

Further developments in the field of X-ray spectroscopy applied to catalysis science are nowadays focused in multiple aspects. Most importantly, improvements in the experimental time resolution are necessary for deep insight knowledge of many chemical processes. For this, a range of complementary X-ray sources is necessary due to timescale changes in the chemical

environment of the atomic species that extend over a wide time range from femtoseconds up to a few seconds. Therefore, a lot of expectation is associated with new, large-scale X-ray facilities being under development worldwide. A new synchrotron sources, like MAXIV in Sweden, are expected to deliver ultrabright X-ray pulses with pulse durations from tens of picoseconds down to sub-picoseconds times. Recently developed fourth-generation X-ray sources – X-ray free electrons lasers – pushed the time limit down to femto-second timescales. The two operating XFELs (LCSL, USA and SACLA, Japan) as well as those under construction (EuXFEL, Germany and SwissFEL, Switzerland) provide a unique opportunity to access timescales of charge-transfers and the following bond-breaking and bond-making mechanism. On the other hand, in order to fully explore capabilities of those new X-ray sources, further developments on X-ray spectroscopy techniques is necessary together with progress on sample delivery/treatments schemes for in situ investigations. Finally, further advancement and evolution in the field of X-ray spectrometers and detectors will be crucial in order to fully explore opportunities provided by the subpicoseconds and femtoseconds X-ray probes.

## Author details

Jakub Szlachetko<sup>1\*</sup> and Jacinto Sá<sup>2</sup>

\*Address all correspondence to: [jakub.szlachetko@psi.ch](mailto:jakub.szlachetko@psi.ch)

1 Paul Scherrer Institute, Switzerland & Institute of Physics, Jan Kochanowski University of Kielce, Poland

2 Department of Chemistry, Uppsala University, Sweden & Institute of Physical Chemistry, Polish Academy of Sciences, Poland

## References

- [1] [http://web.anl.gov/catalysis-science/publications/CAT\\_rpt.pdf](http://web.anl.gov/catalysis-science/publications/CAT_rpt.pdf)
- [2] a) B. Hammer, J. K. Nørskov, *Nature* 376 (1995) 238; b) B. Hammer, J. K. Nørskov, *Adv. Catal.* 45 (2000) 71; c) F. H. B. Lima, J. Zhang, M. H. Shao, K. Sasaki, M. B. Vukmirovic, E. A. Ticianelli, R. R. Adzic, *J. Phys. Chem. C* 111 (2007) 404; d) U. Heiz, E. L. Bullock, *J. Mater. Chem.* 14 (2004) 564; e) W. M. C. Sameera, F. Maseras, *WIREs Comput. Mol. Sci.* 2 (2012) 375.
- [3] a) M. Tada, S. Murata, T. Asakoka, K. Hiroshima, K. Okumura, H. Tanida, T. Uruga, H. Nakanishi, S.-i. Matsumoto, Y. Inada, M. Nomura, Y. Iwasawa, *Angew. Chem. Int. Ed.* 46 (2007) 4310; b) J. Zhang, K. Sasaki, E. Sutter, R. R. Adzic, *Science* 315 (2007) 220.

- [4] J. Szlachetko, M. Nachtegaal, E. de Boni, O. Safonova, J. Sá, G. Smolentsev, M. Szlachetko, J. A. van Bokhoven, J.-C. Dousse, J. Hoszowska, Y. Kayser, P. Jagodzinski, A. Bergamaschi, B. Schmid, C. David, A. Lücke, *Rev. Sci. Instrum.* 83 (2012) 103105.
- [5] a) H. Johann, *Z. Phys.*, 1931, 69, 185; b) E. Kleymenov, J. A. van Bokhoven, C. David, P. Glatzel, M. Janousch, R. Alonso-Mori, M. Studer, M. Willmann, A. Bergamaschi, B. Henrich, M. Nachtegaal, *Rev. Sci. Instrum.*, 82 (2011) 065107.
- [6] J. Sá, J. Szlachetko, *Catal. Lett.* 144 (2014) 197.
- [7] J. L. Calmpbell, *At. Data Nucl. Data Tables* 77 (2001) 50.
- [8] D. Sokaras et al., *Rev. Sci. Instr.* 84, (2013) 053102.
- [9] M. Kavcic et al., *Rev. Sci. Instr.* 83 (2012) 033113.
- [10] T. Johannson, *Z. Phys.* 71 (1932) 705.
- [11] L. von Hamos, *Naturwiss.* 20 (1932) 705.
- [12] R. Alonso-Mori et al., *Rev. Sci. Instr.* 83, (2012) 073114.
- [13] For example, Special Issue on: Progress in Resonant Inelastic X-ray Scattering, *J. Electron Spectroscopy Related Phenomena*, 188, 1-182 (2013) and refs. therein.
- [14] C. J. Sparks, *Phys. Rev. Lett.* 33 (1974) 262, H. Hayashi et al., *Chem. Phys. Lett.* 371 (2003) 125, H. Hayashi et al., *Phys. Rev. B* 68 (2003) 045122, J. Szlachetko et al., *Phys. Rev. Lett.* 97 (2006) 073001, J. Szlachetko et al., *Phys. Rev. A* 75 (2007) 022512.
- [15] J. Tulkki, T. Aberg, *J. Phys. B: At. Mol. Phys.* 15 (1982) L435.
- [16] M. Kavcic et al., *Phys. Rev. B* 87 (2013) 075106.
- [17] S. Eisebitt et al., *Phys. Rev. B* 47 (1993) 14103.
- [18] J. Szlachetko, J. Sá, *Cryst. Eng. Comm.* 15 (2013) 2583.
- [19] a) L. J. Antila, F. G. Santomauro, L. Hammarström, D. L. A. Fernandes, J. Sá, *Chem. Commun.* 51 (2015) 10914; b) J. Sá, P. Friedli, R. Geiger, P. Lerch, M. H. Rittmann-Frank, C. J. Milne, J. Szlachetko, F. G. Santomauro, J. A. van Bokhoven, M. Chergui, M. J. Rossi, H. Sigg, *Analyst* 138 (2013) 1966; c) P. Friedli, H. Sigg, J. Sá, *Photochem. Photobiol. Sci.* 13 (2014) 1393.
- [20] a) A. L. Ankudinov, B. Ravel, J. J. Rehr, S. D. Conradson, *Phys. Rev B* 58 (1998) 7565; b) J. J. Rehr, R. C. Albers, *Rev. Mod. Phys.* 72 (2000) 621; c) A. L. Ankudinov, J. J. Rehr, J. Low, S. R. Bare, *Phys. Rev. Lett.* 86 (2001) 1642.
- [21] a) J. Szlachetko, M. Pichler, D. Pergolosi, J. Sá, T. Lippert, *RSC Adv.* 4 (2014) 11420; b) J. Szlachetko, K. Michalow, M. Nachtegaal, J. Sá, *J. Chem. Sci.* 126 (2014) 511.
- [22] P. N. Rylander, *Catalytic Hydrogenation over Platinum Metals* (1967) Academic Press, New York.

- [23] R. L. Augustine, *Heterogeneous Catalysis for the Synthetic Chemist*, (1996), pp. 315–343, Marcel Dekker, New York.
- [24] a) P. Sabatier, J. B. Sendrens, *Comptes Rendus Hebdomadaires des Seances de l'Academie des Science* 128 (1899) 1173; b) P. Sabatier, J. B. Sendrens, *Comptes Rendus Hebdomadaires des Seances de l'Academie des Science* 130 (1900) 1781.
- [25] a) H. Lindlar, *Helv. Chim. Acta* 35 (1952) 446; b) H. Lindlar, R. Dubuis, *Org. Synth.* 45 (1966) 89.
- [26] a) W. S. Knowles, *Angew. Chem. Int. Ed.* 41 (2002) 1998; b) R. Noyori, *Angew. Chem. Int. Ed.* 41 (2002) 2008.
- [27] M. Crespo-Quesada, A. Yarulin, M. Jin, Y. Xia, L. Kiwi-Minsker, *J. Am. Chem. Soc.* 133 (2011) 12787.
- [28] E. Schmidt, A. Vargas, T. Mallat, A. Baiker, *J. Am. Chem. Soc.* 131 (2009) 12358.
- [29] C. Chapuis, D. Jacoby, *Appl. Catal. A* 221 (2001) 93.
- [30] a) M. Raney, Method of producing finely-divided nickel (1927) U.S. patent 1,628,190; b) T.-K. Yang, D.-S. Lee, J. Haas, *e-EROS Encyclopedia of Reagents for Organic Synthesis* (2006) doi:10.1002/047084289X.rr001.pub2
- [31] Y. Urushibara, *Bull. Chem. Soc. Jpn* 25 (1952) 280.
- [32] <http://catalysts.evonik.com/product/catalysts/en/catalyst-brands/products/activated-base-metal-catalysts/pages/default.aspx>
- [33] a) W. Bonrath, et al. Process for the preparation of saturated aliphatic ketones (2006) Worldwide Patent WO2006029737; b) T. Kawaguchi, et al. 2,3,5-Trimethylhydroquinone (1973) German Patent DE2250066.
- [34] For example: a) B. H. Wu, H. Q. Huang, J. Yang, N. F. Zheng, G. Fu, *Angew. Chem. Int. Ed.* 51 (2012) 3440; b) M. S. Ide, B. Hao, M. Neurock, R. J. Davis, *ACS Catal.* 2 (2012) 671.
- [35] a) A. Saadi, R. Merabti, Z. Rassoul, M.M. Bettahar, *J. Mol. Catal. A* 253 (2006) 79; b) F. Salman, C. Park, R. T. K. Baker, *Catal. Today* 53 (1999) 385; c) W. Lin, *J. Catal.* 303 (2013) 110; d) V. Gutiérrez, F. Nador, G. Radivoy, M. A. Volpe, *Appl. Catal. A* 464-465 (2013) 109.
- [36] H. G. Manyar, B. Yang, H. Daly, H. Moor, S. McMonagle, Y. Tao, G. D. Yadav, A. Goguet, P. Hu and C. Hardacre, *ChemCatChem* 5 (2013) 506.
- [37] H. G. Manyar, R. Morgan, K. Morgan, B. Yang, P. Hu, J. Szlachetko, J. Sá, C. Hardacre, *Catal. Sci. Technol.* 3 (2013) 1497.
- [38] M. Makosch, C. Kartusch, J. Sañol, R. B. Duarte, J. A. van Bokhoven, K. Kvashnina, P. Glatzel, J. Szlachetko, D. L. A. Fernandes, E. Kleymenov, M. Nachtegaal, K. Hungerbühler, *Phys. Chem. Chem. Phys.* 14 (2012) 2164.



- [39] P. Glatzel, J. Singh, K. O. Kvashnina, J. A. van Bokhoven, *J. Am. Chem. Soc.* 132 (2010) 2555.
- [40] O. V. Safonova, M. Tromp, J. A. van Bokhoven, F. M. F. de Groot, J. Evans, P. Glatzel, *J. Phys. Chem. B* 110 (2006) 16162.
- [41] J. Sá, J. Szlachetko, M. Sikora, M. Kavčič, O. V. Safonova, Maarten Nachtegaal, *Nano-scale* 5 (2013) 8462.
- [42] J. Sá, Y. Kayser, U. Hartfelder, C. J. Milne, D. L. A. Fernandes, J. Szlachetko, *Phys. Chem. Chem. Phys.* 16 (2014) 7692.
- [43] J. Szlachetko, J. Sá, M. Nachtegaal, U. Hartfelder, J.-C. Dousse, J. Hoszowska, D. L. A. Fernandes, H. Shi, C. Stampfl, *J. Phys. Chem. Lett.* 5 (2014) 80.
- [44] M. Haruta, T. Kobayachi, H. Sano and N. Yamada, *Chem. Lett.* (1987) 405.
- [45] a) A. Goguet, M. Ace, Y. Saih, J. Sá, J. Kavanagh, C. Hardacre, *Chem. Commun.* (2009) 4889; b) J. Sá, A. Goguet, S. F. R. Taylor, R. Tiruvalam, C. J. Kiely, M. Nachtegaal, G. J. Hutchings, C. Hardacre, *Angew. Chem. Int. Ed.* 50 (2011) 8912.
- [46] J. Szlachetko, J. Sá, M. Nachtegaal, U. Hartfelder, J.-C. Dousse, J. Hoszowska, D. L. A. Fernandes, H. Shi, C. Stampfl, *J. Phys. Chem. Lett.* 5 (2014) 80.
- [47] M. Zienkiewicz, J. Szlachetko, C. Lothschütz, M. Hodorowicz, A. Jabłońska-Wawrzycka, J. Sá, B. Barszcz, *Dalton Trans.* 42 (2013) 7761.
- [48] M. Zienkiewicz, A. Jabłońska-Wawrzycka, J. Szlachetko, Y. Kayser, K. Stadnicka, W. Sawka-Dobrowolska, J. Jezierska, B. Barszcz, J. Sá, *Dalton Trans.* 43 (2014) 8599.
- [49] A. Fujishima, K. Honda, *Nature* 238 (1972) 37.
- [50] K. Hashimoto, H. Irie, A. Fujishima, *JpnJ. Appl. Phys.* 44 (2005) 8269.
- [51] R. Asahi, T. Morikawa, T. Ohwaki, K. Aoki, Y. Taga, *Science* 293 (2001) 269.
- [52] a) B. O'Regan, M. Grätzel, *Nature* 353 (1991) 737; b) M. Grätzel, *Nature* 414 (2001) 338.
- [53] For example: a) K. R. Catchpole, A. Polman, *Opt. Exp.* 16 (2008) 21793; b) M. D. Brown, T. Suteewong, R. S. Kumar, V. D'Innocenzo, A. Petrozza, M. M. Lee, U. Wiesner, H. J. Snaith, *Nano Lett.* 11 (2011) 438; c) L. M. Peter, *J. Phys. Chem. Lett.* 2 (2011) 1861.
- [54] a) Y. Nishijima, K. Ueno, Y. Yokota, K. Murakoshi, H. Misawa, *J. Phys. Chem. Lett.* 1 (2010) 2031; b) F. Wang, N. A. Melosh, *Nano Lett.* 11 (2011) 5426; c) Y. Tian, T. Tatsu-  
ma, *J. Am. Chem. Soc.* 127 (2005) 7632.
- [55] a) P. Christopher, H. Xin, S. Linic, *Nat. Chem.* 3 (2011) 467; b) D. Tsukamoto, Y. Shir-  
aishi, Y. Sugano, S. Ichikawa, S. Tanaka, T. Hirai, *J. Am. Chem. Soc.* 134 (2012) 6309;  
c) P. Christopher, H. Xin, A. Marimuthu, S. Linic, *Nat. Mater.* 11 (2012) 1044; d) S. Lin-

- ic, P. Christopher, D. B. Ingram, *Nat. Mater.* 10 (2011) 911; e) Z. Zhang, J. E. Sader M. L. Roukes, *Nano Lett.* 13 (2013) 14.
- [56] G. L. Hallett-Tapley, M. J. Silvero, M. González-Béjar, M. Grenier, J. C. Netto- Ferreira, J. C. Scaiano, *J. Phys. Chem. C* 115 (2011) 10784.
- [57] M. L. Brongersma, N. J. Halas, P. Nordlander, *Nat. Nanotechnol.* 10 (2015) 25.
- [58] S. Mubeen, J. lee, N. Singh, S. Krämer, G. D. Stucky, M. Moskovits, *Nat. Nanotechnol.* 8 (2013) 247.
- [59] J. Sá, G. Tagliabue, P. Friedli, J. Szlachetko, M. H. Rittmann-Frank, F. G. Santomauro, C. J. Milne, H. Sigg, *Energy Environ. Sci.* 6 (2013) 3584.
- [60] A. Furube, L. Du, K. Hara, R. Katoh, M. Tachiya, *J. Am. Chem. Soc.* 129 (2007) 14852.
- [61] J. Szlachetko, M. Nachtegaal, J. Sá, J.-C. Dousse, J. Hoszowska, E. Kleymenov, M. Janousch, O. V. Safonova, J. A. van Bokhoven, *Chem. Commun.* 48 (2012) 10898.
- [62] J. Szlachetko, M. Nachtegaal, E. de Boni, O. Safonova, J. Sá, G. Smolentsev, M. Szlachetko, J. A. van Bokhoven, J.-C. Dousse, J. Hoszowska, Y. Kayser, P. Jagodzinski, A. Bergamaschi, B. Schmid, C. David, A. Lücke, *Rev. Sci. Instrum.* 83 (2012) 103105.
- [63] W. Błachucki, J. Szlachetko, J. Hoszowska, J.-Cl. Dousse, Y. Kayser, M. Nachtegaal, J. Sá, *Phys. Rev. Lett.* 112 (2014) 173003.
- [64] J. Szlachetko, D. Ferri, V. Marchionni, A. Kambolis, O. V. Safonova, C. J. Milne, O. Kröcher, M. Nachtegaal, J. Sá, *J. Am. Chem. Soc.* 135 (2013) 19071.
- [65] J. Sá, *Recycl. Catal.* 2 (2015) 23.

